

# Fast matrix-free methods for model-based personalized synthetic MR imaging

Subrata Pal, Somak Dutta and Ranjan Maitra

## Abstract

Synthetic Magnetic Resonance (MR) imaging predicts images at new design parameter settings from a few observed MR scans. Model-based methods, that use both the physical and statistical properties underlying the MR signal and its acquisition, can predict images at any setting from as few as three scans, allowing it to be used in individualized patient- and anatomy-specific contexts. However, the estimation problem in model-based synthetic MR imaging is ill-posed and so regularization, in the form of correlated Gaussian Markov Random Fields, is imposed on the voxel-wise spin-lattice relaxation time, spin-spin relaxation time and the proton density underlying the MR image. We develop theoretically sound but computationally practical matrix-free estimation methods for synthetic MR imaging. Our evaluations demonstrate superior performance of our methods in currently-used clinical settings when compared to existing model-based and deep learning methods. Moreover, unlike deep learning approaches, our fast methodology can synthesize needed images during patient visits, with good estimation and prediction accuracy and consistency. An added strength of our model-based approach, also developed and illustrated here, is the accurate estimation of standard errors of regional contrasts in the synthesized images. A R package `symr` implements our methodology.

## Index Terms

Alternating Expectation Conditional Maximization algorithm, Bloch transform, deep image prior, Lanczos algorithm, multi-layered Gaussian Markov Random Field, profile likelihood, variance estimation.



## 1 INTRODUCTION

Magnetic Resonance (MR) Imaging (MRI) [1]–[3] is a noninvasive radiologic tool for understanding tissue structure and function. In MRI, each tissue type has a distinctive spin-lattice or longitudinal relaxation time ( $T_1$ ), spin-spin or transverse relaxation time ( $T_2$ ), and proton density ( $\rho$ ). These quantities are observed only indirectly through noise-contaminated measurements of their transformations that modulate their effect through user-controlled design parameters such as echo time (TE), repetition time (TR) or flip angle ( $\alpha$ ). The exact way in which  $\rho$ ,  $T_1$  and  $T_2$  combine with the design parameters to form an MR image depends on the imaging sequence used [4]–[6]. For example, in spin-echo MRI (where  $\alpha = 90^\circ$ ), the noiseless MR intensity  $\nu_{ij}$  at the  $i$ th voxel and  $j$ th design parameter setting ( $TE_j, TR_j$ ) is approximately specified by the Bloch equation

$$\nu_{ij} = \rho_i \exp\left(-\frac{TE_j}{T_{2i}}\right) \left\{1 - \exp\left(-\frac{TR_j}{T_{1i}}\right)\right\}. \quad (1)$$

In reality, the observed MR signal is noise-contaminated and complex-valued, but its magnitude ( $r_{ij}$ , at the  $i$ th voxel and  $j$ th design parameter setting) is commonly stored, and is well-modeled by a Rice distribution [7]–[11] with density

$$\varrho(r_{ij}; \sigma_j, \nu_{ij}) = \frac{r_{ij}}{\sigma_j^2} \exp\left(-\frac{r_{ij}^2 + \nu_{ij}^2}{2\sigma_j^2}\right) \mathbb{I}_0\left(\frac{r_{ij}\nu_{ij}}{\sigma_j^2}\right), \quad (2)$$

for  $r_{ij} > 0$ . Here  $\sigma > 0$  is the scale parameter of the Rice density and  $\mathbb{I}_k(\cdot)$  is the modified Bessel function of the first kind of order  $k$ . The distribution of  $r_{ij}$  follows from the approximate distribution [12] of the complex-valued MR signal as bivariate Gaussian with mean  $(\nu_{ij} \cos \eta, \nu_{ij} \sin \eta)$  and homogeneous diagonal dispersion matrix  $\sigma^2 \mathbf{I}_2$ , for some  $\eta$ . For identifiability and convenience, we use  $\eta = 0$  [13]–[15].

For a spin-echo MR imaging sequence [16], [17], different (TE, TR) values modulate  $T_1$ ,  $T_2$  and  $\rho$  and can be used to enhance the clinical distinction between tissues. However, the optimal (TE, TR)-settings are patient- and/or anatomy-specific and not always known in advance. Further, patient discomfort or technological challenges can preclude the acquisition of images at some settings [14], [18]. These shortcomings were sought to be overcome using *synthetic MRI* (syMRI) [19]–[23], where the underlying  $\rho$ ,  $T_1$ , and  $T_2$  values at each voxel are estimated using a set of *training* images, and then inserted along with unobserved (TE, TR,  $\alpha$ )-values into (1) to obtain corresponding synthetic images. The technique is an appealing alternative in situations requiring images at multiple settings and/or long acquisition times, such as in pediatric imaging of the developing brain or in non-cooperating subjects [24]–[27]. However, despite its vast potential, syMRI's clinical adaptation has been stymied by the inherent ill-posedness of the inversion of the Bloch equation, which leads to unstable solutions [14], or by the inordinate times taken by palliative measures such as regularization using Markov Random Field (MRF) priors [28], [29]. Deep learning (DL) methods were developed [30], but they require substantially

large training images that are impractical in a clinical single-subject personalized setting. Recently, [31] developed a DIPsynMRI framework based on a “deep image prior” [32] that works well in personalized settings with only three training images. However, besides being computationally slow, these DL methods do not easily provide any measure of prediction uncertainty. An alternative model-based approach proposed by [14], while practical, used the one-step late Expectation-Maximization (EM), or OSL-EM algorithm [33] that is not guaranteed to converge, and, as shown in this paper, can provide sub-optimal estimates.

In this paper, we instead develop (Section 2) a scalable alternating expectation conditional maximization (AECM) algorithm [34] for synthetic MRI that is guaranteed to converge and essentially matches the speed of non-regularized methods such as LS. The key ingredients of our AECM algorithm are a checkerboard coloring scheme [35], [36] that allows fast parallel block maximization over the voxel-wise parameters and analytically profiles out some of the Gaussian MRF (GMRF) parameters, reducing the optimization over the remaining parameters to be of at most two variables. An additional appealing aspect of our model-based approach is the conceptual ease of obtaining standard errors (SEs) of our predictions, for which we also provide methods for their fast implementation. Section 3 evaluates properties of our estimates, and demonstrates our methodology on a normal subject in a clinical setting. We also investigate the selection of test sets for optimizing predictive performance and demonstrate consistency of our synthetic MRI predictions. A separate set of simulation experiments evaluates estimation and prediction accuracy and consistency for different noise levels. We conclude with some discussion. An online supplement with sections, figures and tables prefixed by ‘S’, is available. Our methods are implemented in a R [37] package *symr* (pronounced *sim·mer*) that uses openMP-based parallelization for computational practicality.

## 2 METHODOLOGY

### 2.1 A penalized likelihood model for syMRI

Following [14], the observed image intensities  $\mathbf{R} = \{r_{ij}\}$  are assumed to be independent Rice-distributed random variables with density (2). We get the loglikelihood

$$\ell(\{T_{1i}, T_{2i}, \rho_i\}_{i=1}^n; \mathbf{R}) = \sum_{i=1}^n \sum_{j=1}^m \log \varrho(r_{ij}; \nu_{ij}, \sigma_j), \quad (3)$$

where the voxels  $i = 1, 2, \dots, n$  are embedded in a regular 3D array of  $n_x \times n_y \times n_z$  voxels. The noise parameter  $\sigma_j^2$  in each training image is estimated using [15]. As in [14], we spatially regularize  $(\rho, T_1, T_2)$  by the voxel-wise transformations  $W_{i1} = \rho_i$ ,  $W_{i2} = \exp(-1/T_{1i})$ , and  $W_{i3} = \exp(-1/T_{2i})$  and penalizing (3) to obtain the optimization problem

$$\max_{\mathbf{W}} \{ \ell(\mathbf{W}; R) - \frac{1}{2} \text{Tr} \Psi^{-1} \mathbf{W}' \Lambda \mathbf{W} \}. \quad (4)$$

In (4),  $\mathbf{W} = (W_{ik})$  is a  $n \times 3$  matrix,  $\Psi$  is a  $3 \times 3$  positive definite matrix and  $\Lambda = \beta_z \mathbf{J}_{n_z} \otimes \mathbf{I}_{n_y} \otimes \mathbf{I}_{n_x} + \beta_y \mathbf{I}_{n_z} \otimes \mathbf{J}_{n_y} \otimes \mathbf{I}_{n_x} + \beta_x \mathbf{I}_{n_z} \otimes \mathbf{I}_{n_y} \otimes \mathbf{J}_{n_x}$ , where  $\beta_x, \beta_y$ , and  $\beta_z$  are nonnegative parameters,  $\mathbf{I}_k$  is the identity matrix of order  $k$ , and  $\mathbf{J}_k$  is the  $k \times k$  tri-diagonal matrix with all nonzero off-diagonals as  $-1$ , the first and the last diagonal entries both as  $1$  and the other diagonal entries all as  $2$ . For all practical purpose,  $n = n_x n_y n_z$  is large, and  $\Lambda$  is an enormous but sparse matrix, with each row having at most seven non-zero elements, corresponding to the two neighbors in each direction and the voxel itself. The penalty in (4) can be written as the kernel of the (improper) matrix normal density

$$f(\mathbf{W}; \Psi, \beta) = \frac{|\Lambda|_+^{3/2} \exp\{-\frac{1}{2} \text{Tr}(\Psi^{-1} \mathbf{W}' \Lambda \mathbf{W})\}}{(2\pi)^{3n/2} |\Psi|^{n/2}}, \quad (5)$$

where  $|\Lambda|_+$  is the product of the positive eigenvalues of  $\Lambda$ . The Kronecker structure in the components of  $\Lambda$  means that  $\Psi$  and  $\beta = (\beta_x, \beta_y, \beta_z)$  need constraints for identifiability. Though there are many options, we impose the constraint that  $2\beta_x + 2\beta_y + 2\beta_z = 1$ , from the alternative specification of (5) as the (improper) density of a first order intrinsic multi-layer GMRF [35], [38], [39]. If  $\mathbf{W}'_i$  is the  $i$ th row (corresponding to the  $i$ th interior voxel) of  $\mathbf{W}$ , then the conditional distribution of  $\mathbf{W}_i$  given  $\mathbf{W}_{-i}$  (all other rows of  $\mathbf{W}$ ) is trivariate normal with conditional mean and variance

$$\mathbb{E}(\mathbf{W}_i | \mathbf{W}_{-i}) = - \sum_{q \heartsuit i} \Lambda_{iq} \mathbf{W}_q, \quad \text{Var}(\mathbf{W}_i | \mathbf{W}_{-i}) = \Psi, \quad (6)$$

where  $q \heartsuit i$  if and only if voxel  $q$  is a neighbor of voxel  $i$ , and  $\Lambda_{iq}$  is the  $(i, q)$ th element of  $\Lambda$ . Similar expressions exist for boundary voxels. Further,  $\Lambda_{iq} = -\beta_x, -\beta_y$  or  $-\beta_z$  if  $q \heartsuit i$  in the  $x$ -,  $y$ - or  $z$ -direction, so (6) characterizes  $\mathbb{E}(\mathbf{W}_i | \mathbf{W}_{-i})$  as the weighted average of its neighboring  $\mathbf{W}_q$  values with weights  $\beta_x, \beta_y$  or  $\beta_z$ . The conditional covariance is constant.

### 2.2 Matrix-free AECM for parameter estimation

#### 2.2.1 Background

Analytical or numerical optimization in (4) is well-nigh impractical because of the intractability introduced by the penalty term. A EM algorithm can conceptually be developed from the generative model of the Rice distribution of the individual

$r_{ij}$ s. Specifically, with  $r_{ij}$  as the observed magnitude, we let  $\theta_{ij}$  be the (missing) phase angle, then  $(r_{ij} \cos \theta_{ij}, r_{ij} \sin \theta_{ij})$  is bivariate normally distributed with mean  $(\nu_{ij}, 0)$  and variance-covariance matrix  $\sigma_j^2 \mathbf{I}_2$ . Then, ignoring terms not involving  $\nu_{ij}$ , the complete log-likelihood is  $\sum_{i=1}^n \sum_{j=1}^m \sigma_j^{-2} (r_{ij} \nu_{ij} \cos \theta_{ij} - \nu_{ij}^2/2)$ . The algorithm iteratively computes, in the expectation step (E-step), the expectation of the complete loglikelihood given the observations, and evaluated at the current parameter values, while the maximization step (M-step) maximizes the result. We now list the two steps.

2.2.1.1 E-step: The E-step requires the conditional expectation of each  $\cos \theta_{ij}$  given  $r_{ij}$  at the current values  $(\mathbf{W}^{(t)}, \Psi^{(t)}, \beta^{(t)})$  of  $(\mathbf{W}, \Psi, \beta)$ . We compute and define

$$Z_{ij}^{(t)} := \mathbb{E}[\cos \theta_{ij} | r_{ij}; \nu_{ij}^{(t)}] = \mathbb{A}_1 \left( r_{ij} \nu_{ij}^{(t)} / \sigma_j^2 \right),$$

where  $\mathbb{A}_1(x) := \mathbb{I}_1(x)/\mathbb{I}_0(x)$ . Here,  $Z_{ij}^{(t)}$  is free of  $\beta^{(t)}$  or  $\Psi^{(t)}$ , but rather, depends only on  $\nu_{ij}^{(t)}$  which only involves the  $i$ th row of  $\mathbf{W}^{(t)}$ . So  $Z_{ij}^{(t)}$ s can be computed in parallel without any data racing by allocating an instance of  $\sigma_j^2$  to every processor thread.

2.2.1.2 M-Step: At the  $(t+1)$ th iteration, updates  $(\mathbf{W}^{(t+1)}, \Psi^{(t+1)}, \beta^{(t+1)})$  are obtained by maximizing

$$Q^*(\mathbf{W}, \Psi, \beta; \mathbf{W}^{(t)}) = Q(\mathbf{W}; \mathbf{W}^{(t)}) + \log f(\mathbf{W}; \Psi, \Lambda) \quad (7)$$

with respect to (w.r.t.)  $(\mathbf{W}, \Psi, \beta)$ , with

$$Q(\mathbf{W}; \mathbf{W}^{(t)}) = \sum_{i=1}^n \sum_{j=1}^m \sigma_j^{-2} \left( -\frac{1}{2} \nu_{ij}^2 + r_{ij} \nu_{ij} Z_{ij}^{(t)} \right). \quad (8)$$

In (8),  $\nu_{ij}$  is again a function only of the  $i$ th row of  $\mathbf{W}$ . However, optimization of  $Q^*$  is still challenging so [14] employed an OSL-EM algorithm [33]. Specifically, they solved  $\nabla Q(\mathbf{W} | \mathbf{W}^{(t)}) + \nabla \log f(\mathbf{W}^{(t)}; \Psi, \beta) = 0$  in  $(\mathbf{W}, \Psi, \beta)$ . This equation can be decomposed into those involving only the individual rows of  $\mathbf{W}$ , greatly simplifying computation. (The equations for  $\Psi$  and  $\beta$  are still joint.) However, unlike the EM algorithm, OSL-EM is neither guaranteed to converge [14], nor increase the penalized log-likelihood monotonically at each iteration (see Figure S1 for an illustration where OSL-EM actually reduces the penalized log-likelihood providing a sub-optimal estimate). So, we describe and implement an AECM algorithm that is guaranteed to converge monotonically to a local maximum.

## 2.2.2 Development and implementation

An AECM algorithm [34] partitions the parameter space and splits the M-step into conditional maximization (CM) steps, one for each element in the above partition, and alternates the E-step with each CM step. In our framework, we exploit the GMRF structure underlying  $\mathbf{W}$  to color the voxels as black or white using a checkerboard pattern [35] so that no two neighboring voxels have the same color. Then our parameter space is partitioned into three sets, with two partitions for the  $\mathbf{W}$ s at the black and white voxels and the third partition containing  $(\Psi, \beta)$ . Then each partition is updated in its CM-step while keeping the variables in the other partitions fixed at their current values.

Our bifurcation of  $\mathbf{W}$  is driven by the fact that the CM-step for  $\mathbf{W}$  at each black (or white) voxel involves fixed values from only the neighboring white (correspondingly black) voxels. So the optimization problems over the black (white) voxels are *embarrassingly* parallel and are efficiently implemented with no data races in computer memory. Our race-negligible parallel optimization is explicitly given by

**Proposition 1.** Maximizing  $Q^*(\mathbf{W}, \Psi, \beta; \mathbf{W}^{(t)})$  w.r.t.  $\mathbf{W}_i$  for fixed  $(\Psi, \beta)$  and  $\mathbf{W}_{-i}$  is equivalent to maximizing

$$Q_i^*(\mathbf{W}_i) = \sum_{j=1}^m \frac{1}{\sigma_j^2} \left( -\nu_{ij}^2/2 + r_{ij} \nu_{ij} Z_{ij}^{(t)} \right) - \sum_{q \heartsuit i} \Lambda_{i,q} \mathbf{W}_q' \Psi^{-1} \mathbf{W}_i - \frac{1}{2} \Lambda_{i,i} \mathbf{W}_i' \Psi^{-1} \mathbf{W}_i, \quad (9)$$

with gradient vector w.r.t.  $\mathbf{W}_i$  given by

$$\nabla Q_i^*(\mathbf{W}_i) = \sum_{j=1}^m \frac{1}{\sigma_j^2} \left( -\nu_{ij} + r_{ij} Z_{ij}^{(t)} \right) \nabla \nu_{i,j} - \sum_{q \heartsuit i} \Lambda_{i,q} \Psi^{-1} \mathbf{W}_q - \Lambda_{i,i} \Psi^{-1} \mathbf{W}_i. \quad (10)$$

Here,  $\nabla \nu_{i,j}$  is the gradient vector of  $\nu_{i,j}$  w.r.t.  $\mathbf{W}_i$ .

*Proof.* See Section B-A. □

Proposition 1 yields a small 3D optimization problem that we efficiently solve using the quasi-Newton box-constrained L-BFGS-B algorithm with limited memory calculations for the Hessian matrix [40], [41]. The box constraints are obtained from the ranges of  $\mathbf{W}$ . Further, the part of (A2) that is inside the parenthesis, is needed to be computed only once per iteration per voxel using sparse matrix computations and the last term can be computed many times inside the L-BFGS-B algorithm as the algorithm explores the space. Also, to have more stable ratios of Bessel functions in the expression for  $Z_{ij}^{(t)}$ , we have used exponentially scaled Bessel functions [42], as in [15], and resorted to a Taylor series expansion as the argument tends to  $\infty$ .

Next, for fixed  $\mathbf{W}$ , we describe how to update the estimates of  $(\Psi, \beta)$ . The following proposition shows that given  $\beta$ ,  $\Psi$  can be analytically profiled out giving a simple objective function only in  $\beta$ .

**Proposition 2.** Fix  $\mathbf{W} = \mathbf{W}^{(t+1)}$ . For fixed  $\beta$ , the function  $\Psi \rightarrow Q^*(\mathbf{W}, \Psi, \beta; \mathbf{W})$  is maximized at  $\hat{\Psi} = n^{-1}\mathbf{W}'\mathbf{\Lambda}\mathbf{W}$  (with  $\mathbf{\Lambda} \equiv \mathbf{\Lambda}(\beta)$ ). The resulting profile function for  $\beta$  is

$$Q_p^*(\beta) = c + \frac{3}{2} \log |\mathbf{\Lambda}|_+ - \frac{n}{2} \log |\mathbf{W}'\mathbf{\Lambda}\mathbf{W}| \quad (11)$$

where  $c$  is a constant that depends only on  $n$  but not on  $\beta$ .

*Proof.* See Section B-B. □

(11) and its derivative require calculation of  $|\mathbf{\Lambda}|_+$  and the determinant of a  $3 \times 3$  matrix  $\mathbf{W}'\mathbf{\Lambda}\mathbf{W}$ . but these are easily obtained by noting that the eigenvalues of  $\mathbf{J}_k$  [39] are

$$\lambda_i = 2 [1 - \cos \{\pi(i-1)/k\}] \text{ for } i = 1, 2, \dots, k. \quad (12)$$

Let  $\mathbf{D}_k$  be the vector of eigenvalues of  $\mathbf{J}_k$  ( $k = n_x, n_y, n_z$ ). Then  $|\mathbf{\Lambda}|_+$  is a product of the elements of the vector  $\beta_x \mathbf{1}_{n_z} \otimes \mathbf{1}_{n_y} \otimes \mathbf{D}_{n_x} + \beta_y \mathbf{1}_{n_z} \otimes \mathbf{D}_{n_y} \otimes \mathbf{1}_{n_x} + \beta_z \mathbf{D}_{n_z} \otimes \mathbf{1}_{n_y} \otimes \mathbf{1}_{n_x}$ . Our matrix-free treatment of  $(\Psi, \beta)$  is a faster, more elegant and easier-implemented contrast to [14] where  $\Psi$  is further parametrized via a Cholesky factorization and updated along with  $\beta$  using another L-BFGS-B algorithm.

Like OSL-EM, we initialize  $\mathbf{W}$  in our AECM algorithm with the LS estimates, and obtain initial values of  $\Psi$  and  $\beta$ , as per Proposition 2. Unlike OSL-EM, our AECM algorithm is guaranteed to converge [34], as also shown in Figure S1.

### 2.2.3 Generating synthetic images

The estimated  $(\rho, T_1, T_2)$ , obtained from the terminating  $\mathbf{W}$ s, are inserted along with desired design parameter settings into (1) to synthesize spin-echo images. Similar methods can be employed for other MRI pulse sequences.

## 2.3 Matrix-free standard error computations

An attractive feature of our model-based approach and the use of penalized likelihood estimators is the provision for “on-the-fly” calculation of SEs. We now provide the theoretical development and fast implementation for calculating SEs of contrasts of regions of interest (ROIs) in synthetic images  $\hat{\nu}$ .

Following [43] or [44], the estimated observed penalized information matrix for  $\mathbf{W}$  is given by  $\hat{\Omega} = \hat{\mathbf{H}} + \hat{\mathbf{\Lambda}} \otimes \hat{\Psi}^{-1}$ , where  $\hat{\mathbf{H}}$  is the negative of the Hessian of the observed log-likelihood (3) with respect to  $\mathbf{W}$  evaluated at  $\hat{\mathbf{W}}$  (see Section SI-A),  $\hat{\mathbf{\Lambda}}$  is the  $\mathbf{\Lambda}$  matrix evaluated at the terminating  $\hat{\beta}$ , and  $\hat{\Psi}$  is also obtained from the terminated AECM algorithm. Thus,  $\hat{\mathbf{H}}$  is a  $3n \times 3n$  block-diagonal matrix (with entries corresponding to the background voxels set to zero). The approximate dispersion matrix of a synthetic image  $\hat{\nu}$  is calculated from  $\hat{\Omega}$  by the multivariate delta method to be  $\mathbf{S} = \nabla \hat{\nu} \hat{\Omega}^{-1} \nabla \hat{\nu}'$  where  $\nabla \hat{\nu}$  is the  $n \times 3n$  Jacobian matrix of  $\nu$  with respect to  $\mathbf{W}$  evaluated at  $\hat{\mathbf{W}}$ . The computation of  $\mathbf{S}$  is challenging but can be parallelized. Moreover, in practice, we are mostly interested in calculating means and SEs of ROIs drawn on synthetic images. The SE of a linear combination  $\mathbf{c}'\hat{\nu}$  of the voxel-wise values of a synthetic image is  $\text{SE}(\mathbf{c}'\hat{\nu}) = (\mathbf{c}'\mathbf{S}\mathbf{c})^{1/2} = \{(\mathbf{c}'\nabla \hat{\nu})\hat{\Omega}^{-1}(\nabla \hat{\nu}'\mathbf{c})\}^{1/2}$ .

The computation of  $\text{SE}(\mathbf{c}'\hat{\nu})$  still presents substantial numerical challenges. In particular, it requires us to solve an equation of the form  $\hat{\Omega}\mathbf{x} = \mathbf{d}$  where  $\mathbf{d} = (\nabla \hat{\nu})'\mathbf{c}$ . Although  $\hat{\Omega}$  is sparse, it is typically so large that standard methods based on sparse matrix factorization (e.g. sparse Cholesky decomposition) run out of memory mainly because they suffer from fill-ins. In our example, even the heuristic methods [45, Ch. 8] for reducing fill-ins failed to provide a factorization in machines with as much as 384GB RAM. So we use the matrix-free Lanczos algorithm [39] to solve the system. Specifically, we initialize as  $\theta_1 = \|\mathbf{d}\|$ ,  $\mathbf{v}_1 = \mathbf{d}/\theta_1$ ,  $\mathbf{w}_1 = \hat{\Omega}\mathbf{v}_1$ ,  $\kappa_1 = \mathbf{v}_1'\mathbf{w}_1$ ,  $\gamma_1 = \sqrt{\kappa_1}$ ,  $\phi_1 = \theta_1/\gamma_1$ ,  $\mathbf{h}_1 = \mathbf{v}_1/\gamma_1$  and set the initial solution:  $\mathbf{x}_1 = \phi_1\mathbf{h}_1$ . Next, for  $i = 2, 3, \dots$ , we set

- $\theta_i = \|\mathbf{w}_{i-1} - \kappa_{i-1}\mathbf{v}_{i-1}\|$ .
- $\mathbf{v}_i = (\mathbf{w}_{i-1} - \kappa_{i-1}\mathbf{v}_{i-1})/\theta_i$ .
- $\mathbf{w}_i = \hat{\Omega}\mathbf{v}_i - \theta_i\mathbf{v}_{i-1}$ .
- $\kappa_i = \mathbf{v}_i'\mathbf{w}_i$ ,  $\delta_i = \theta_i/\gamma_{i-1}$ , and  $\gamma_i = \sqrt{\kappa_i - \delta_i^2}$ .
- $\phi_i = -\delta_i\phi_{i-1}/\gamma_i$  and  $\mathbf{h}_i = (\mathbf{v}_i - \delta_i\mathbf{h}_{i-1})/\gamma_i$ .

and update the solution:  $\mathbf{x}_i = \mathbf{x}_{i-1} + \phi_i\mathbf{h}_i$  till convergence, that is declared if the relative error  $\|\hat{\Omega}\mathbf{x}_i - \mathbf{d}\|/\theta_1$  is below some pre-specified tolerance.

By carefully recycling the memory space for  $\mathbf{v}_i$ s and  $\mathbf{w}_i$ s, the Lanczos algorithm requires only  $\mathcal{O}(n)$  memory in addition to the storage for  $\hat{\Omega}$ . Also,  $\hat{\Omega}$  is used only through the matrix-vector product  $\hat{\Omega}\mathbf{v}_i$  which can be computed fast with  $\mathcal{O}(n)$  computational complexity. Finally, while we may use an incomplete Cholesky preconditioner to accelerate convergence of the Lanczos iterations [39], our examples showed that a simple diagonal preconditioner achieves at least the same computing speed, and is often faster.

We conclude our discussion of SE estimation of regional contrasts in synthesized MR images by noting that its feasibility stems from our use of a direct model-based approach. Such an approach is not possible with the deep learning methods

of [31] because of the intractability of the estimation. Moreover, a parametric bootstrap approach to obtain SEs is not computationally feasible given the time taken (over a day) to obtain estimates from one training set. In contrast, our AECM estimates take not even minutes to obtain, which means that they, along with regional contrast SEs, can be obtained and used during a patient visit.

This section has developed a computationally practical AECM algorithm for generating synthetic MR images from as few as three training images, and a method for fast computations of the SEs of ROI contrasts in such images.

### 3 PERFORMANCE EVALUATIONS

We illustrate our AECM methodology and evaluate its performance. Our studies are on the only known 3D dataset collected on the same subject at multiple (TE,TR) test set values (in addition to the training set) that permits evaluation of predictions [14], [31], and for greater understanding, on simulated datasets from the Brainweb interface [46]. (See Table S1 for the design parameter settings at which the dataset: the images are indexed accordingly.)

From each training set of three images, we estimated  $\rho$ ,  $T_1$ ,  $T_2$  using OSL-EM (OSL), DIPSynMRI (DL), and AECM, and then inserted them into (1) to synthesize images at the test set values. Additionally, at the suggestion of a reviewer, we also evaluated performance of our methodology when (2) is approximated by a Gaussian distribution with mean  $\nu_{ij}$  and standard deviation  $\sigma_j$ . The penalty remains unchanged, and is (5). In this scenario, the penalized maximum likelihood estimator is the same as the Penalized Least Squares (PLS) estimator (and referred to in this paper as such). Further, the estimation algorithm is then simply a block-coordinate descent method (note that we minimize the PLS), and the obtained estimates are again used along with (1) to synthesize images at the desired test set values.

Whether obtained by OLS, DL, AECM or PLS, the predicted synthetic images were compared to the test set images using the scaled root mean squared prediction error (RMSPE) for the  $j$ th image volume, given by  $s_j^{-1} \sqrt{\sum_{i=1}^n (r_{ij} - \hat{\nu}_{ij})^2 / n}$ , where  $s_j$  is the standard deviation of the foreground voxel values in  $j$ th acquired image. Note that our evaluations calculated  $\hat{\nu}_{ij}$  in the (scaled) RMSPE calculations in  $\hat{\nu}_{ij}$  in two ways. First, we used  $\hat{\nu}_{ij}$  without accounting for the Rice distribution of the voxel-wise predictions. In the second case, we set  $\hat{\nu}_{ij}^* = \hat{\sigma}_j \sqrt{\pi/2} \mathbb{L}_{1/2}(-\hat{\nu}_{ij}^2 / \hat{\sigma}_j^2)$ , or the mean of the Rice distribution with parameters  $\hat{\nu}_{ij}$  and  $\hat{\sigma}_j$ , with  $\mathbb{L}_{1/2}(x) = e^{x/2} [(1-x)\mathbb{I}_0(-x/2) - x\mathbb{I}_1(-x/2)]$  denoting the Laguerre polynomial of order 1/2. However, the RMSPEs in each case were essentially the same, so we report our measures using the predicted  $\hat{\nu}_{ij}$ . Also, our computations were done in parallel on a 2.3GHz Intel(R) Xeon(R) Gold 6140 processor, capable of handling up to 36 threads.

#### 3.1 Real Dataset

The dataset was acquired [14] on a 1.5T Signa scanner using a spin-echo imaging sequence at a resolution of  $1.15\text{mm} \times 1.15\text{mm} \times 7.25\text{mm}$  in a field of view set to be  $294\text{mm} \times 294\text{mm} \times 145\text{mm}$ . For each 3D image volume,  $n_x = n_y = 256$  and  $n_z = 20$ . Figure 1 displays the 10th slice of the training set images. Figure S1 shows the value of (4) as the OSL-EM and

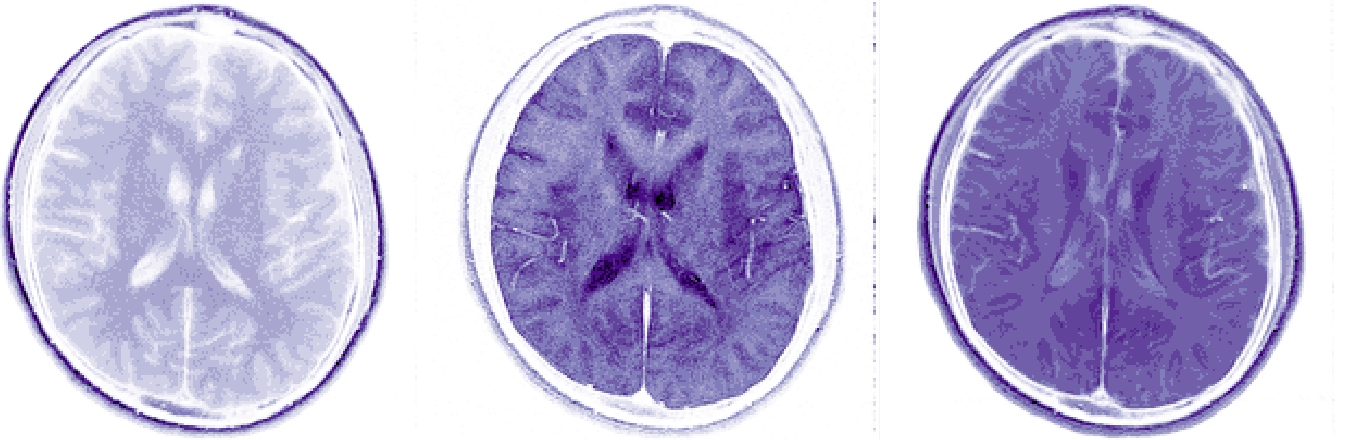


Fig. 1. Mid-axial view of the training set images with (from left to right) TE/TR = 0.01/0.6, 0.08/2, 0.01/3 (seconds).

AECM algorithms proceed from LS initialization. In this example, OSL-EM is seen to have an uncertain trajectory, and on the whole, goes down after the first iteration. On the other hand, AECM correctly increases and terminates in a few iterations. Our implementation of AECM ensures that this accuracy does not come at a price, with estimation and synthetic image generation typically done in about a minute. Further, the AECM shows greater stability with respect to different initial values than OSL-EM.

Figure 2 displays the performance in terms of the RMSPE, of the competing methods on the eight acquired (TE, TR) settings.

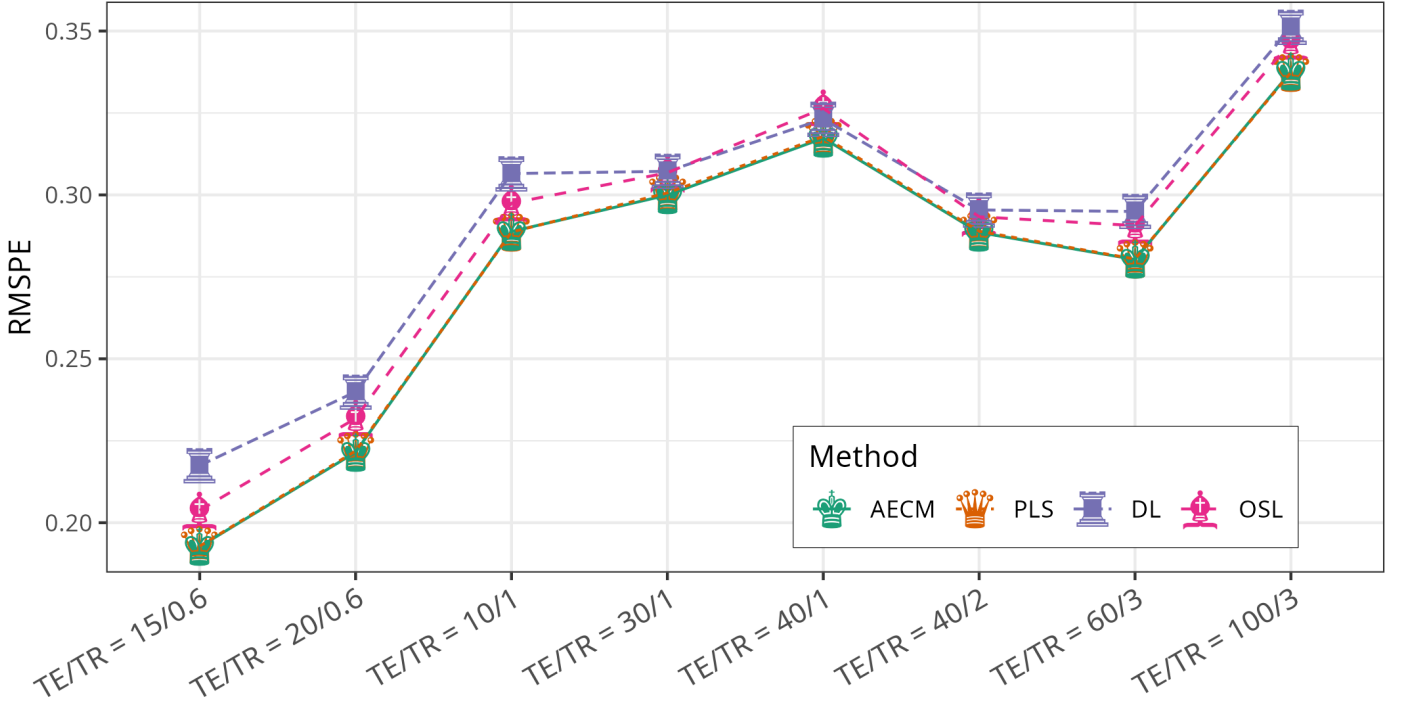


Fig. 2. RMPSEs on the eight test images for the different methods.

We see that AECM is the best performer at all settings, closely followed by PLS. Figure 3 displays the performance of OSL, DL, PLS and AECM at a sample setting. A closer inspection of the OSL and DL synthetic MR images indicate greater disagreement from the truth, than with the AECM and PLS image. Further, following [14], we also considered performance of the AECM methodology in synthesizing MR images as the number of images in the training set is increased. Figure S2 in Section SII-D shows improvement of the performances over the best set of images, indicating consistency of our methodology.

### 3.1.1 Estimating SEs of ROI means

We also evaluated our estimated SEs of ROI means of synthetic images obtained using the training set of the real data. We considered three ROIs consisting of Cerebro-Spinal Fluid (CSF), Gray Matter (GM) and White Matter (WM). Table 1 provides the ROI means of the synthetically generated variances. The machinery of Section 2.3 was used to estimate SEs of the ROI means and compared with computationally expensive bootstrap estimates. (For details, see Section SII-B, which also shows insignificant differences between our estimates and the bootstrap-estimated SEs.)

Note also that in the AECM case, the bootstrap-estimated SEs are computationally expensive to obtain, but not prohibitive as in the case of SEs of DL-estimated regional means because the DL-estimation procedure would take almost a day for each bootstrap replication. In contrast, our AECM estimate takes a few minutes.

TABLE 1  
Estimated CSF, GM and WM ROI means in synthetic images and their SEs:  $\hat{\sigma}_s$ s calculated using the formula in Section 2.3, and  $\hat{\sigma}_b$ s estimated using parametric bootstrap. The scale for the SEs is  $\times 10^{-3}$ .

Image	CSF			GM			WM		
	Mean	$\hat{\sigma}_s$	$\hat{\sigma}_b$	Mean	$\hat{\sigma}_s$	$\hat{\sigma}_b$	Mean	$\hat{\sigma}_s$	$\hat{\sigma}_b$
2	36.7	3.73	4.45	73.1	3.31	3.71	123.4	7.53	6.93
3	33.8	3.95	4.15	67.9	3.05	3.41	111.4	7.07	6.61
4	57.7	5.11	5.62	112.7	4.09	4.62	167.1	7.73	7.38
5	42.0	4.13	4.35	84.0	2.99	3.28	110.5	6.22	6.07
6	36.3	3.85	4.07	72.8	2.74	2.95	90.0	6.44	6.52
7	88.4	5.55	5.70	164.0	3.96	4.23	191.4	9.86	9.52
8	55.9	4.44	4.51	106.4	2.79	2.77	102.7	7.21	7.24
11	52.6	5.42	5.41	93.4	3.59	3.73	69.8	7.44	7.80
12	33.3	5.13	4.69	54.5	3.39	3.49	31.1	5.74	6.18

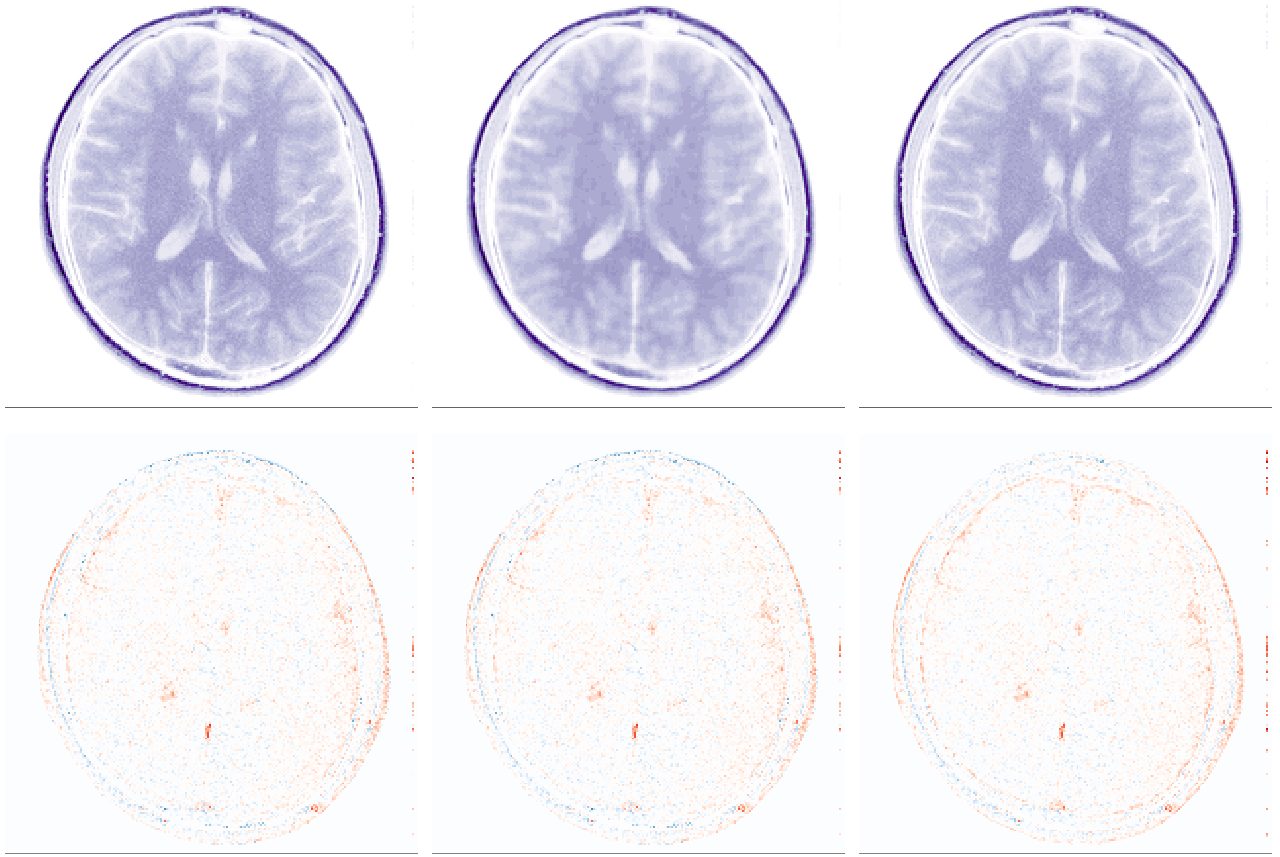


Fig. 3. (Top) Mid-axial views of the OSL, DL and AECM-synthesized images for  $TE/TR = 15/0.6$ , along with (bottom) the differenced image (from the acquired image) at that setting.

### 3.1.2 Choice of Optimal Training Set

Following [14], we investigate all possible  $(TE, TR)$  triplets to see the best choice for synthesizing images. For each possible set of three training images, we obtained LS, OSL-EM and AECM-estimated parameters and then obtained synthetic images for the rest images considered test set. Section SII-C shows that the best synthetic images are indeed obtained when we have  $\rho-$ ,  $T_1-$ , and  $T_2-$ weighted images as the triplet of training images.

## 3.2 Simulation Experiments

Our next set of experiments is on prediction accuracy relative to noise. We demonstrate and evaluate performance of our methodology on images obtained at a  $1\text{mm} \times 1\text{mm} \times 5\text{mm}$  resolution with  $181 \times 217 \times 36$  voxels and simulated using the Brainweb interface [46]. This tool simulates realistic images at  $TE$ ,  $TR$ , and flip angle settings, slice thicknesses, noise levels, and intensity nonuniformity (INU) proportions. We collected training images from Brainweb’s “mild” and “severe” multiple sclerosis lesions databases and used them in a simulated spin-echo MR sequence with the same three  $(TE, TR)$  parameters and noise levels  $\{1\%, 2.5\%, 5\%, 7.5\%, 10\%\}$ . Separately, we acquired spin-echo training images with 1% noise for the same  $(TE, TR)$  parameters to investigate the influence of field inhomogeneity at  $\{0\%, 5\%, 10\%\}$  INU (of so-called field A) levels. We acquired noiseless “ground truth” images from the Brainweb interface at 0% INU levels and nine  $(TE, TR)$ s to evaluate our predicted synthetic images.

We compared the predicted synthetic images at the nine (unshaded)  $(TE, TR)$  values of RMSPE of the predicted synthetic MRIs for the “mild” MS dataset in Figure 4. We see that the AECM provides better prediction accuracy than OSL and at a given setting and also beats PLS. At lower noise, AECM outperforms DL, while DL outperforms AECM for higher noise. The performances for the “severe” MS dataset and other scenarios are described in Section SII-E. Our performance evaluations indicate our AECM approach can improve synthetic MRI both in simulation and real data settings. Further, AECM comparable to LS method in terms of time and better in terms of performances. It is far quicker than DL (with AECM taking about a minute, and the latter taking almost a day), synthesizing images in real time and yielding superior results in realistic low-noise situations.

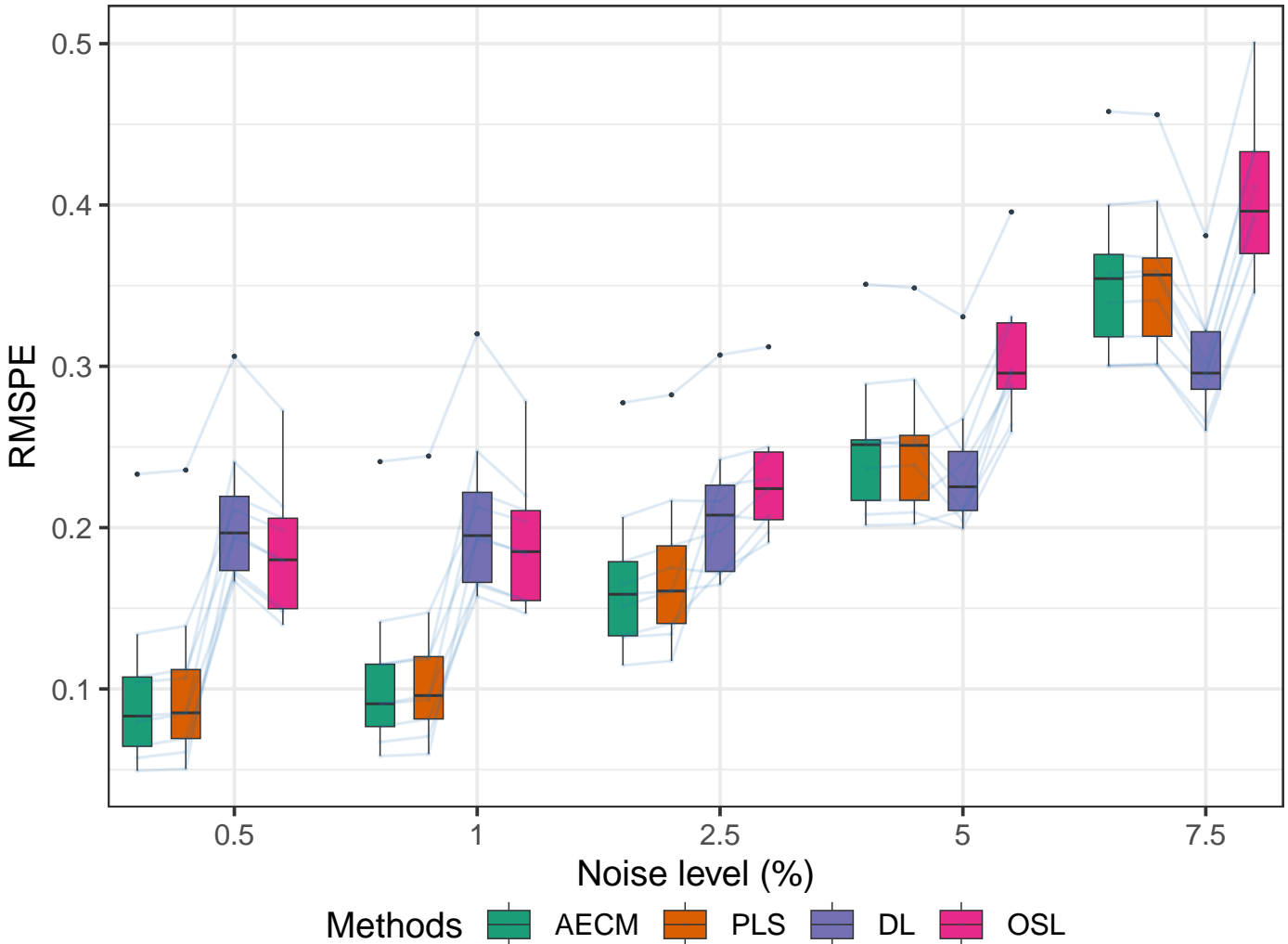


Fig. 4. RMSPE values for different noise of Brainweb simulated data for different methods for “mild” MS dataset. The lines in the linked boxplot connect the different datasets.

## 4 DISCUSSION

We have provided a computationally practical but theoretically sound implementation of model-based synthetic MR imaging that can enable its use patient-specific settings. Our approach penalizes the Rice-distribution based loglikelihood through a transformed GMRF [14] with parameters estimated via a matrix-free AECM scheme, that unlike OSL-EM, is guaranteed to solve (4) locally. Over different simulations, the block-descent-optimization-based PLS gives comparable results, but is edged out by AECM. Further, while PLS estimates are obtained at about half the time as AECM estimates, the latter itself takes less than a couple of minutes, even on a large image volume, and is practical to apply in a clinical setting, and can be obtained and interpreted during a patient visit. With the same resources, the DL-based method took about a day. Experimental evaluations also show AECM to have better overall performance over even DL-based synthetic MR, at substantial lower cost. An added benefit of our model-based approach is the ready availability of SE estimates, for which we also provide practical matrix-free computations. Our experiments show our estimates to be nonsignificantly distinct from those bootstrap-obtained values. Compute costs make parametric bootstrap-estimated SEs impractical to implement for the DL-based method where (approximate) analytical expressions for the regional contrast SEs are also not readily obtained.

A reviewer has asked about the context of our results in light of [47]’s findings that Ricean-based activation tests in functional Magnetic Resonance Imaging (fMRI) analysis are only superior to Gaussian-approximation-based tests for small signal-to-noise ratios (SNRs) of less than 0.6, typically much smaller than what is seen in practice. We note that those findings are on activation detection and under the assumption of independence in the fMRI time series. Indeed, [48] demonstrated that using the original Gaussian complex-valued data (which forms the basis of the Ricean model for the magnitudes) and an  $AR(p)$  temporal dependence and a general covariance structure for the real and imaginary errors, showed greater power of activation than using a Gaussian  $AR(p)$  model on the magnitude data. (Subsequent recent work in [49] supports these findings also for the Rice-distributed time series data.) Finally, we note that our methods here can benefit MRI data acquired at higher resolution, since voxel volume is inversely proportional to SNR [48]. Therefore, we



believe that the use of the more accurate Rice model (2) over its Gaussian approximation has value, especially in the context of higher-resolution synthetic MRI studies.

Both reviewers have asked about the feasibility of our method with penalties more general than the first order MRF in (5). For such neighborhood structures (e.g., higher order MRFs) on  $\mathbf{W}$ , the partitioning of  $\mathbf{W}$  needs to be done through coding sets [35] or cliques [50] that generalize the checkerboard bifurcation. Succinctly, for higher order MRFs, voxels can be partitioned into disjoint sets  $\mathcal{C}_1, \mathcal{C}_2, \dots, \mathcal{C}_l$  for some  $l \in \mathbb{N}$  so that for each  $j$ ,  $\{\mathbf{W}_i : i \in \mathcal{C}_j\}$  are conditionally independent random variables given the rest. Consequently, the optimization problems on each  $\mathcal{C}_j$  ( $1 \leq j \leq l$ ) remain embarrassingly parallel. Further, the eigenvalues of the matrix  $\mathbf{\Lambda}$  are analytically known for many of these higher order MRFs [51] on 2D lattice, and we surmise these can be also computed in 3D.

There are some other issues that could benefit from further attention. For instance, transformations beyond the ones used in transforming  $(\rho, T_1, T_2)$  to  $(\mathbf{W}_1, \mathbf{W}_2, \mathbf{W}_3)$  could be investigated. Also of interest may be the choice of penalty functions that go beyond stationary GMRFs. The use of practical Bayesian methodology incorporating ingredients of our matrix-free approach may also be worth exploring.

## ACKNOWLEDGMENTS

A portion of this article won the first author a 2023 Student Paper Competition award from the American Statistical Association (ASA) Section on Statistical Computing and Graphics. The research of the first and third authors was supported in part by the National Institute of Biomedical Imaging and Bioengineering (NIBIB) of the National Institutes of Health (NIH) under Grant R21EB034184. The content of this paper is however solely the responsibility of the authors and does not represent the official views of the NIBIB or the NIH.

## REFERENCES

- [1] L. M. Katims, "Nuclear magnetic resonance imaging: methods and current status," *Medical Instrum.*, vol. 16, no. 4, pp. 213–6, 1982.
- [2] P. Mansfield and P. G. Morris, *NMR Imaging in Biomedicine*. New York: Academic Press, 1982.
- [3] W. S. Hinshaw and A. H. Lent, "An introduction to NMR imaging: From the Bloch equation to the imaging equation," *Proceedings of the IEEE*, vol. 71, no. 3, pp. 338–350, 1983.
- [4] V. Kuperman, *Magnetic Resonance Imaging: Physical Principles and Applications*, 1st ed. San Diego, California: Academic Press, 2000.
- [5] M. A. Bernstein, K. F. King, and X. J. Zhou, Eds., *Handbook of MRI Pulse Sequences*. Burlington: Academic Press, 2004.
- [6] R. W. Brown, Y.-C. N. Cheng, E. M. Haacke, M. R. Thompson, and R. Venkatesan, Eds., *Magnetic Resonance Imaging: Physical Principles and Sequences*, 2nd ed. Hoboken, New Jersey: John Wiley & Sons, Ltd, 2014.
- [7] R. M. Henkelman, "Measurement of signal intensities in the presence of noise in mr images," *Medical Physics*, vol. 12, no. 2, pp. 232–233, 1985.
- [8] J. Sijbers, "Signal and noise estimation from magnetic resonance images," Ph.D. dissertation, University of Antwerp, 1998.
- [9] J. Sijbers, A. J. den Dekker, J. Van Audekerke, M. Verhoye, and D. Van Dyck, "Estimation of the noise in magnitude MR images," *Magnetic Resonance Imaging*, vol. 16, no. 1, pp. 87–90, 1998.
- [10] S. O. Rice, "Mathematical analysis of random noise," *Bell System Techn. J.*, vol. 23, pp. 282–332, 1944.
- [11] —, "Mathematical analysis of random noise," *Bell System Techn. J.*, vol. 24, pp. 46–156, 1945.
- [12] Y. Wang and T. Lei, "Statistical analysis of MR imaging and its applications in image modeling," in *Proceedings of 1st International Conference on Image Processing*, vol. 1, 1994, pp. 866–870.
- [13] R. Maitra and D. Faden, "Noise estimation in magnitude MR datasets," *IEEE Transactions on Medical Imaging*, vol. 28, no. 10, pp. 1615–1622, 2009.
- [14] R. Maitra and J. J. Riddles, "Synthetic magnetic resonance imaging revisited," *IEEE Transactions on Medical Imaging*, vol. 29, no. 3, pp. 895–902, march 2010.
- [15] R. Maitra, "On the expectation-maximization algorithm for Rice-Rayleigh mixtures with application to estimating the noise parameter in magnitude MR datasets," *Sankhyā: The Indian Journal of Statistics, Series B*, vol. 75, no. 2, p. 293–318, 2013.
- [16] E. L. Hahn, "Spin echoes," *Physical review*, vol. 80, no. 4, p. 580, 1950.
- [17] J. Hennig, A. Nauerth, and H. Friedburg, "RARE imaging – a fast imaging method for clinical MR," *Magnetic Resonance in Medicine*, vol. 3, no. 6, pp. 823–33, 1986.
- [18] S. C. L. Deoni, T. M. Peters, and B. K. Rutt, "High-resolution  $T_1$  and  $T_2$  mapping of the brain in a clinically acceptable time with DESPOT1 and DESPOT2," *Magnetic Resonance in Medicine*, vol. 53, pp. 237–241, 2005.
- [19] S. Bobman, S. Riederer, J. Lee, S. Suddarth, H. Wang, and J. MacFall, "Synthesized MR images: Comparison with acquired images," *Radiology*, vol. 155, pp. 731–8, 1985.
- [20] S. Bobman, S. Riederer, J. Lee, T. Tasciyan, F. Farzaneh, and H. Wang, "Pulse sequence extrapolation with acquired images," *Radiology*, vol. 159, pp. 253–8, 1986.
- [21] D. A. Feinberg, C. M. Mills, J. P. Posin, D. A. Ortendahl, N. M. Hylton, L. E. Crooks, J. C. Watts, L. Kaufman, M. Arakawa, J. C. Hoenninger, and M. Brantz-Zawadski, "Multiple spin-echo Magnetic Resonance Imaging," *Radiology*, vol. 155, pp. 437–42, 1985.
- [22] D. A. Ortendahl, Hylton, L. Kaufman, J. C. Watts, L. E. Crooks, and D. D. Stark, "Analytical tools for Magnetic Resonance Imaging," *Radiology*, vol. 153, no. 2, pp. 479–488, 1984.
- [23] F. G. Gonçalves, S. D. Serai, and G. Zuccoli, "Synthetic brain MRI: review of current concepts and future directions," *Topics in Magnetic Resonance Imaging*, vol. 27, no. 6, pp. 387–393, 2018.
- [24] A. M. Betts, J. L. Leach, B. V. Jones, B. Zhang, and S. Serai, "Brain imaging with synthetic mr in children: clinical quality assessment," *Neuroradiology*, vol. 58, no. 10, pp. 1017–1026, 2016.
- [25] A. McAllister, J. Leach, H. West, B. Jones, B. Zhang, and S. Serai, "Quantitative synthetic MRI in children: normative intracranial tissue segmentation values during development," *American Journal of Neuroradiology*, vol. 38, no. 12, pp. 2364–2372, 2017.
- [26] C. Andica, A. Hagiwara, M. Hori, K. Kamagata, S. Koshino, T. Maekawa, M. Suzuki, H. Fujiwara, M. Ikeno, T. Shimizu *et al.*, "Review of synthetic MRI in pediatric brains: Basic principle of mr quantification, its features, clinical applications, and limitations," *Journal of Neuroradiology*, vol. 46, no. 4, pp. 268–275, 2019.
- [27] A. Hagiwara, M. Hori, K. Yokoyama, M. Takemura, C. Andica, T. Tabata, K. Kamagata, M. Suzuki, K. Kumamaru, M. Nakazawa *et al.*, "Synthetic MRI in the detection of multiple sclerosis plaques," *American Journal of Neuroradiology*, vol. 38, no. 2, pp. 257–263, 2017.
- [28] I. K. Glad and G. Sebastiani, "A Bayesian approach to synthetic Magnetic Resonance Imaging," *Biometrika*, vol. 82, no. 2, pp. 237–250, June 1995.

- [29] R. Maitra and J. E. Besag, "Bayesian reconstruction in synthetic Magnetic Resonance Imaging," in *Bayesian Inference in Inverse Problems*, ser. Proceedings of the Society of Photo-Optical Instrumentation Engineers (SPIE) Meetings, A. Mohammad-Djafari, Ed., vol. 3459, 1998, pp. 39–47.
- [30] A. Hagiwara, Y. Otsuka, M. Hori, Y. Tachibana, K. Yokoyama, S. Fujita, C. Andica, K. Kamagata, R. Irie, S. Koshino *et al.*, "Improving the quality of synthetic flair images with deep learning using a conditional generative adversarial network for pixel-by-pixel image translation," *American Journal of Neuroradiology*, vol. 40, no. 2, pp. 224–230, 2019.
- [31] S. Pal, S. Dutta, and R. Maitra, "Personalized synthetic MR imaging with deep learning enhancements," *Magnetic Resonance in Medicine*, 2022. [Online]. Available: <https://onlinelibrary.wiley.com/doi/abs/10.1002/mrm.29527>
- [32] D. Ulyanov, A. Vedaldi, and V. Lempitsky, "Deep image prior," in *Proceedings of the IEEE conference on computer vision and pattern recognition*, 2018, pp. 9446–9454.
- [33] P. J. Green, "On the use of the EM algorithm for penalized likelihood estimation," *Journal of the Royal Statistical Society: Series B (Methodological)*, vol. 52, pp. 443–452, 1990.
- [34] X.-L. Meng and D. Van Dyk, "The EM algorithm—an old folk-song sung to a fast new tune," *Journal of the Royal Statistical Society: Series B (Statistical Methodology)*, vol. 59, no. 3, pp. 511–567, 1997.
- [35] J. Besag, "Spatial interaction and the statistical analysis of lattice systems," *Journal of the Royal Statistical Society: Series B (Methodological)*, vol. 36, no. 2, pp. 192–225, 1974.
- [36] J. Besag, P. Green, D. Higdon, and K. Mengersen, "Bayesian computation and stochastic systems," *Statistical Science*, vol. 10, no. 1, pp. 3–41, 1995.
- [37] R Core Team, *R: A Language and Environment for Statistical Computing*, R Foundation for Statistical Computing, Vienna, Austria, 2020. [Online]. Available: <https://www.R-project.org/>
- [38] J. Besag and C. Kooperberg, "On conditional and intrinsic autoregressions," *Biometrika*, vol. 82, no. 4, pp. 733–746, 1995.
- [39] S. Dutta and D. Mondal, "An h-likelihood method for spatial mixed linear models based on intrinsic auto-regressions," *Journal of the Royal Statistical Society: Series B: Statistical Methodology*, vol. 77, pp. 699–726, 2015.
- [40] R. H. Byrd, P. Lu, and J. Nocedal, "A limited memory algorithm for bound constrained optimization," *SIAM Journal in Scientific and Statistical Computing*, vol. 16, no. 5, pp. 1190–1208, 1995.
- [41] C. Zhu, R. H. Byrd, P. Lu, and J. Nocedal, "Algorithm 778: L-BFGS-B: Fortran subroutines for large-scale bound-constrained optimization," *ACM Transactions on Mathematical Software (TOMS)*, vol. 23, no. 4, pp. 550–560, 1997.
- [42] M. Abramowitz and I. A. Stegun, *Handbook of Mathematical Functions with Formulas, Graphs, and Mathematical Tables*, Ninth Dover printing, tenth GPO printing ed. New York: Dover, 1964.
- [43] M. R. Segal, P. Bacchetti, and N. P. Jewell, "Variances for maximum penalized likelihood estimates obtained via the EM algorithm," *Journal of the Royal Statistical Society: Series B (Methodological)*, vol. 56, no. 2, pp. 345–352, 1994.
- [44] W. Lee and Y. Pawitan, "Direct calculation of the variance of maximum penalized likelihood estimates via EM algorithm," *The American Statistician*, vol. 68, no. 2, pp. 93–97, 2014.
- [45] T. A. Davis, *Direct methods for sparse linear systems*. SIAM, 2006.
- [46] C. Cocosco, V. Kollokian, R. Kwan, and A. Evans, "Brainweb: Online Interface to a 3D MRI Simulated Brain Database," *NeuroImage*, vol. 5, no. 4, May 1997.
- [47] D. W. Adrian, R. Maitra, and D. B. Rowe, "Ricean over gaussian modelling in magnitude fmri analysis—added complexity with negligible practical benefits," *Stat*, vol. 2, no. 1, pp. 303–316, 2013. [Online]. Available: <https://onlinelibrary.wiley.com/doi/abs/10.1002/sta4.34>
- [48] —, "Complex-valued time series modeling for improved activation detection in fMRI studies," *Annals of Applied Statistics*, vol. 12, no. 3, pp. 1451–1478, 2018.
- [49] —, "Rice-distributed autoregressive time series modeling of magnitude function MRI data," *submitted*, 2023.
- [50] M. S. Kaiser, S. N. Lahiri, and D. J. Nordman, "Goodness of fit tests for a class of Markov random field models," *The Annals of Statistics*, vol. 40, no. 1, pp. 104 – 130, 2012. [Online]. Available: <https://doi.org/10.1214/11-AOS948>
- [51] D. Mondal, "On edge correction of conditional and intrinsic autoregressions," *Biometrika*, vol. 105, no. 2, pp. 447–454, 2018.
- [52] K. V. Mardia, J. T. Kent, and J. M. Bibby, *Multivariate Analysis*. Academic Press Inc., 1979.

## A APPENDIX

### A PROOFS

#### A.1 Proof of Proposition 1

Only the kernel of  $f(\mathbf{W}; \Psi, \Lambda)$  in (5) involves  $\mathbf{W}$  so we have, but for a constant free of  $\mathbf{W}$ ,

$$\log f(\mathbf{W}; \Psi, \Lambda) = -\frac{1}{2} \text{Tr} (\Psi^{-1} \mathbf{W}' \Lambda \mathbf{W}) = -\frac{1}{2} \text{Tr} (\Lambda (\mathbf{W} \Psi^{-1} \mathbf{W}')) = -\frac{1}{2} \sum_p \sum_q \Lambda_{p,q} \cdot \mathbf{W}_q \Psi^{-1} \mathbf{W}'_p. \quad (\text{A1})$$

The portion of (A1) that involves the  $i$ th voxel, and hence  $\mathbf{W}_i$ , is

$$\log f(\mathbf{W}; \Psi, \Lambda) = c - \left( \sum_{q \neq i} \Lambda_{i,q} \mathbf{W}_q \right) \Psi^{-1} \mathbf{W}'_i - \frac{1}{2} \Lambda_{i,i} \mathbf{W}'_i \Psi^{-1} \mathbf{W}_i \quad (\text{A2})$$

which gives us equation (9), with  $c$  a constant not depending on  $\mathbf{W}_i$ . However,  $\Lambda \neq \mathbf{0}$  only if  $q \heartsuit i$ . Applying the chain rule for derivatives, we get the first partial derivative, w.r.t.  $W_{ik}$ , of the  $Q(\mathbf{W}; \mathbf{W}^{(t)})$  of (8) as

$$\frac{\partial Q}{\partial W_{ik}} = \sum_{j=1}^m \sigma_j^{-2} \left( -\nu_{ij} + r_{ij} Z_{ij}^{(t)} \right) \frac{\partial \nu_{ij}}{\partial W_{ik}}, \quad (\text{A3})$$

for which we need the derivatives of (1). For the transformed variable  $\mathbf{W}$ , the Bloch equation is

$$\nu_{ij} = W_{i1} \left\{ 1 - W_{i2}^{\text{TR}_j} \right\} W_{i3}^{\text{TE}_j}, \quad (\text{A4})$$

where from we get the first partial derivatives

$$\frac{\partial \nu_{ij}}{\partial W_{ik}} = \begin{cases} W_{i3}^{\text{TE}_j} \{1 - W_{i2}^{\text{TR}_j}\}, & k=1 \\ -W_{i1} \text{TR}_j W_{i3}^{\text{TE}_j} W_{i2}^{\text{TR}_j-1}, & k=2 \\ W_{i1} \text{TE}_j W_{i3}^{\text{TE}_j-1} \{1 - W_{i2}^{\text{TR}_j}\}, & k=3 \end{cases}$$

and the second partial derivatives

$$\frac{\partial^2 \nu_{ij}}{\partial W_{ik} \partial W_{ik'}} = \begin{cases} 0, & k=1, k'=1 \\ -\text{TR}_j W_{i3}^{\text{TE}_j} W_{i2}^{\text{TR}_j-1}, & k=1, k'=2 \\ \text{TE}_j W_{i3}^{\text{TE}_j-1} (1 - W_{i2}^{\text{TR}_j}), & k=1, k'=3 \\ -W_{i1} \text{TR}_j (\text{TR}_j - 1) W_{i3}^{\text{TE}_j} W_{i2}^{\text{TR}_j-2}, & k=2, k'=2 \\ -W_{i1} \text{TR}_j \text{TE}_j W_{i3}^{\text{TE}_j-1} W_{i2}^{\text{TR}_j-1}, & k=2, k'=3 \\ W_{i1} \text{TE}_j (\text{TE}_j - 1) W_{i3}^{\text{TE}_j-2} (1 - W_{i2}^{\text{TR}_j}), & k=3, k'=3. \end{cases}$$

From the above, we get (10) from (A3) and (A2).

## A.2 Proof of Proposition 2

From (5), we have

$$\begin{aligned} \log f(\mathbf{W}; \Psi, \beta) &= -\frac{1}{2} \text{Tr} (\Psi^{-1} \mathbf{W}' \Lambda \mathbf{W}) + \frac{3}{2} \log |\Lambda|^* - \frac{3n}{2} \log(2\pi) - \frac{n}{2} \log |\Psi| \\ &= -\frac{1}{2} \text{Tr} (\Psi^{-1} \Xi) - \frac{n}{2} \log |\Psi| + K, \end{aligned} \quad (\text{A5})$$

where  $\Xi = (\mathbf{W}' \Lambda \mathbf{W})$  and  $K$  depends only on  $\beta$  and  $n$ .

The optimization of (A5) w.r.t.  $\Psi$  is similar to the problem for finding the maximum likelihood estimator for the variance-covariance matrix in multivariate normal samples as in [52, Theorem 4.2.1]. In our case, the first two terms contain the arithmetic (AM) and the geometric means (GM) of eigenvalues of  $n^{-1} \Psi^{-1} \Xi$ . The AM-GM inequality shows that this expression is maximized at  $\Psi = \Xi/n = (\mathbf{W}' \Lambda \mathbf{W})/n$ . Incorporating this estimated value yields the profile likelihood

$$Q_p^*(\beta) = -\frac{1}{2} \text{Tr} (n \mathbf{I}_3) + \frac{3}{2} \log |\Lambda|^* - \frac{3n}{2} \log(2\pi) - \frac{n}{2} \log \left| \frac{1}{n} \Xi \right| = c + \frac{3}{2} \log |\Lambda|^* - \frac{n}{2} \log |\mathbf{W}' \Lambda \mathbf{W}| \quad (\text{A6})$$

where  $c$  is a constant that involves  $n$ .

## SUPPLEMENTARY INFORMATION

### SI SUPPLEMENTARY MATERIALS FOR THEORY AND METHODS

#### SI.1 Information Matrix

The observed information matrix corresponding to  $\mathbf{W}$  is obtained from (3) and (2). The first partial derivative is similar to (9):

$$\frac{\partial \ell}{\partial W_{ik}} = \sum_{j=1}^m \sigma_j^{-2} \left\{ -\nu_{ij} + r_{ij} \frac{\mathbb{I}_1 \left( \frac{r_{ij} \nu_{ij}}{\sigma_j^2} \right)}{\mathbb{I}_0 \left( \frac{r_{ij} \nu_{ij}}{\sigma_j^2} \right)} \right\} \frac{\partial \nu_{ij}}{\partial W_{ik}},$$

while the second partial derivative is

$$\frac{\partial^2 \ell}{\partial W_{ik'} \partial W_{ik}} = \sum_{j=1}^m \sigma_j^{-2} \left\{ -\nu_{ij} + r_{ij} \frac{\mathbb{I}_1 \left( \frac{r_{ij} \nu_{ij}}{\sigma_j^2} \right)}{\mathbb{I}_0 \left( \frac{r_{ij} \nu_{ij}}{\sigma_j^2} \right)} \right\} \frac{\partial^2 \nu_{ij}}{\partial W_{ik'} \partial W_{ik}} + \sum_{j=1}^m \left\{ -\frac{1}{\sigma_j^2} + \frac{r_{ij}^2}{\sigma_j^4} h \left( \frac{r_{ij} \nu_{ij}}{\sigma_j^2} \right) \right\} \frac{\partial \nu_{ij}}{\partial W_{ik}} \frac{\partial \nu_{ij}}{\partial W_{ik'}}.$$

$\widehat{\mathbf{H}}$  is equal to the negative second derivative w.r.t.  $W_{ik}$  over  $i$  and  $k$ , and  $\mathbb{I}_s(x)$  is the modified Bessel function of the first kind of order  $s$ . Note that, any order of derivative of  $\ell_i$  w.r.t.  $W_{i'k}$  is 0 if  $i \neq i'$ , making  $\widehat{\mathbf{H}}$  block diagonal, and

$$h(x) := \frac{d}{dx} (A_1(x)) = \frac{1}{2} \left[ \frac{\mathbb{I}_0(x) \{ \mathbb{I}_0(x) + \mathbb{I}_2(x) \} - 2\mathbb{I}_1^2(x)}{\mathbb{I}_0^2(x)} \right] \quad (\text{S1})$$

The part of the penalized likelihood from the Rice density contributes to  $\widehat{\mathbf{H}}$ , and the Hessian of the penalty part contributes to  $\Lambda \otimes \Psi^{-1}$ , producing the  $\widehat{\Omega}$  matrix.

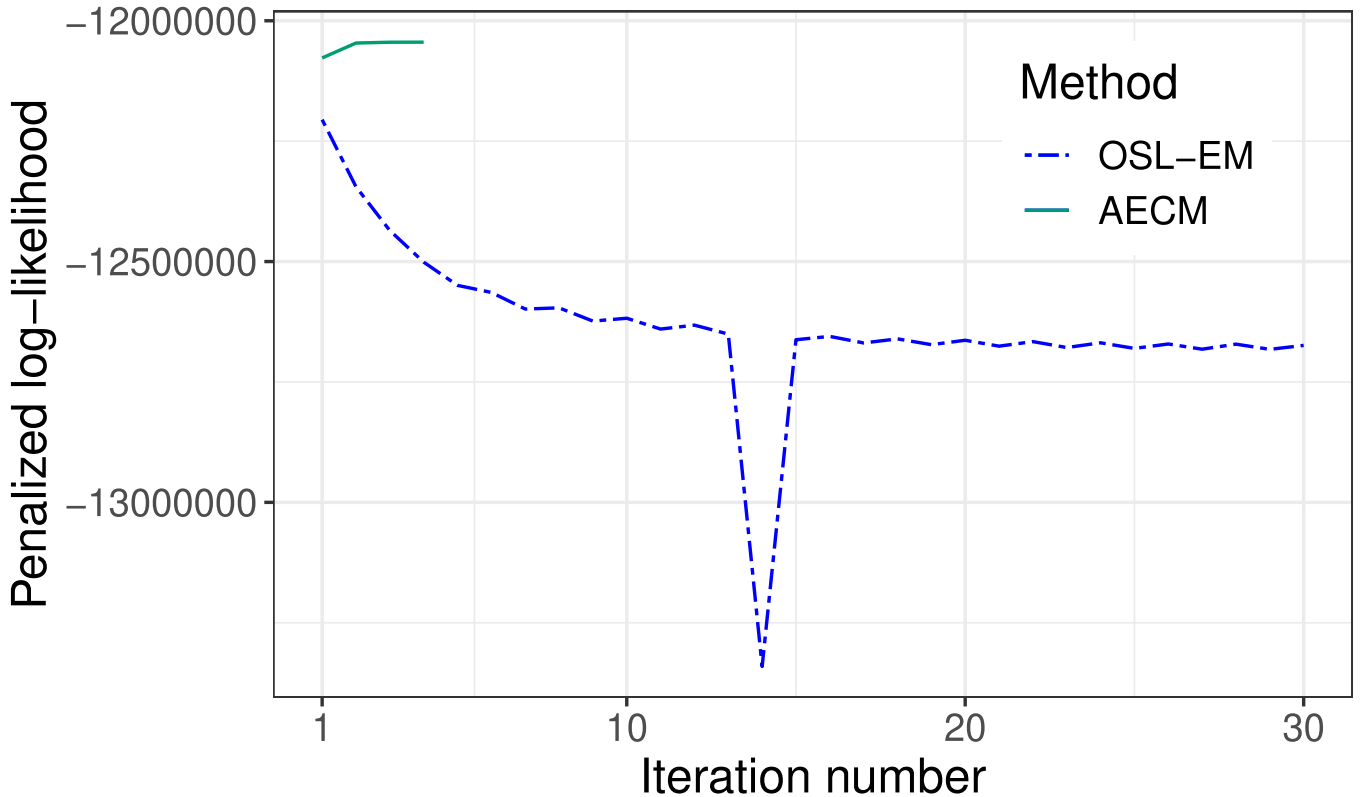


Fig. S1. The path of the objective function in (4), using OSL-EM and AECM.

## SII SUPPLEMENTARY MATERIALS FOR PERFORMANCE EVALUATIONS

### SII.1 The trajectory of the objective function in (4) when using OSL-EM and AECM

Figure S1 shows the path of the objective function in (4) for the example in Section 3.1. We see that the penalized log-likelihood for OSL-EM does not always increase in every iteration. In fact, in this example, it oscillates, especially with increased desired precision in terms of relative error. However, the penalized log-likelihood increases for AECM, as is guaranteed by theory. Further, with the increasing ascent property, the algorithm usually converges with fewer iterations than OSL-EM.

### SII.2 Bootstrap validation of SE calculations

We validate our theoretically derived approximate SEs using the parametric bootstrap. Our bootstrap procedure was as follows. First, using the estimated  $\widehat{W}$ , we obtained resampled training images were generated using the equations (1) and (2) with the train TE and TR settings. For the  $b$ th resampled training images, we used AECM to have estimated  $\widehat{W}_b^*$ ,  $b = 1, 2, \dots, B$ , with  $B$  as the number of bootstrap replications, and inserted them, along with the test (TE, TR) (1) used to get  $\widehat{D}_b$  for these settings. From these resampled synthetic images, the standard deviations of  $c'\widehat{D}_b$ , over  $b = 1, 2, \dots, B$ , can be calculated to provide us with estimated SEs of  $c'\widehat{D}$  which can be compared to our theoretically derived approximate SEs. However, we note that our validator has sampling variability. In order to account for this variability, we calculated the standard deviations of these bootstrap SEs. We used a jackknife-type estimator to estimate this SD. Specifically, from the bootstrap replications, we used a leave-one-out method to get  $B$  leave-one-out bootstrapped SE estimates. The standard deviation over these  $B$  leave-one-out SE estimates can be used to obtain a SE of the bootstrap-estimated SE. Our experiments indicate that the theoretical SEs of the ROI means of the synthetic images are within one SE of the bootstrap-estimated SEs and so are not significantly different.

### SII.3 Choice of Optimal Training Set

Following [14], we also investigate all possible (TE, TR) settings to see if some choice can provide better synthetic images. There are  ${}^{12}C_3 = 220$  possible sets of three training images, but some of them are not distinct and are discarded, leaving behind 212 sets. For each set of three training images, we obtained LS, OSL-EM and AECM-estimated parameters and then obtained synthetic images for the nine (TE, TR)-values outside the considered training set.

Table S1 displays numerical performance of the AECM-estimated synthetic images for the top 10 combinations (ordered according to the increasing scaled RMSPE), and shows the per cent improvement of AECM and OSL-EM over LS for each of the measures. We see around 5% improvement of AECM over LS. Once again, OSL-EM is unpredictable in its improvement over LS, often doing worse.

TABLE S1

The 12 (TE, TR) settings (in seconds) for the data, and the ten best training sets, their performance measures for the LS estimates, and their average performance measures relative to the LS estimates ( $\times 0.01$ ). In the table, OSL and AE denote OSL-EM and AECM-estimated predictions.

j	1	2	3	4	5	6	7	8	9	10	11	12	
Settings	TE	0.01	0.015	0.02	0.01	0.03	0.04	0.01	0.04	0.08	0.01	0.06	0.1
	TR	0.6	0.6	0.6	1.0	1.0	1.0	2.0	2.0	2.0	3.0	3.0	3.0

Training Images	LS performance measure				RMSPE				MAPE			
	RMSPE		MAPE		$\hat{\nu}$		$\hat{\nu}^*$		$\hat{\nu}$		$\hat{\nu}^*$	
	$\hat{\nu}$	$\hat{\nu}^*$	$\hat{\nu}$	$\hat{\nu}^*$	OSL	AE	OSL	AE	OSL	AE	OSL	AE
1, 9, 10	20.93	20.92	24.89	24.89	-0.44	1.10	-0.34	1.98	-0.26	1.28	0.01	1.20
2, 9, 10	21.11	21.10	25.08	25.07	-0.64	1.28	-0.50	2.41	-0.47	1.49	-0.09	1.44
2, 10, 12	21.60	21.60	25.71	25.70	-1.19	0.95	-1.54	1.76	-1.21	1.00	-0.80	0.95
2, 7, 9	21.38	21.35	25.34	25.32	0.68	3.42	1.53	6.55	1.23	3.51	1.32	3.44
1, 10, 12	21.64	21.64	25.77	25.77	-0.90	1.12	-1.26	1.92	-1.09	1.15	-0.81	1.03
1, 7, 9	21.54	21.54	25.54	25.54	0.14	2.97	0.77	5.78	0.65	2.96	0.87	2.94
1, 8, 9	21.54	21.53	24.97	24.96	0.19	3.82	0.85	7.36	-0.12	3.46	0.10	3.41
1, 10, 11	21.86	21.83	25.83	25.81	0.02	1.05	0.57	2.01	0.15	1.08	0.36	1.05
2, 10, 11	21.91	21.89	25.89	25.86	-0.21	1.27	0.26	2.44	-0.13	1.43	0.19	1.40
2, 8, 9	21.60	21.59	25.05	25.04	-0.00	3.24	0.59	6.35	-0.38	3.03	-0.09	3.02

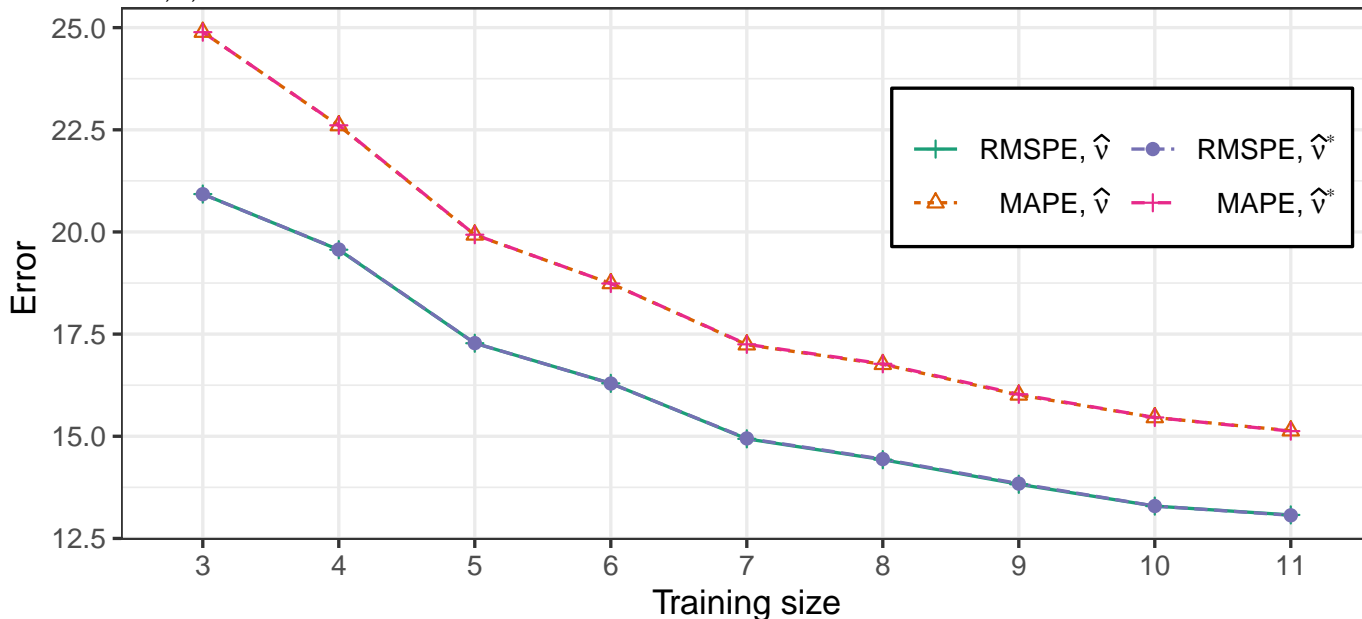


Fig. S2. The best training samples for varying training sample sizes and their performance measures.

#### SII.4 Consistency of Statistical Methods

A desirable feature of any estimation or prediction method is statistical consistency, or improvement in performance as more information (training image set) becomes available. Therefore, we considered and evaluated performance of the AECM method in generating synthetic images as the number of images in the training set increased over  $m \in \{3, 4, 5, \dots, 11\}$ . For each  $m$ , we evaluated predictive performance with a training set of images of all possible training image set combinations of size  $m$  and compared them with the remaining images in the test sample. The RMSPE and MAPE values for the best set, and for each  $m$  are displayed in Figure S2 and show consistency of our synthetic image generation method.

#### SII.5 Performance measures for the Brainweb data under different conditions

Figure S3 shows a similar set of performance measures as in 4, but with “severe” MS dataset with various noise percentages.

We have also evaluated our methods for various INU level, which is presented in the Figure S4.

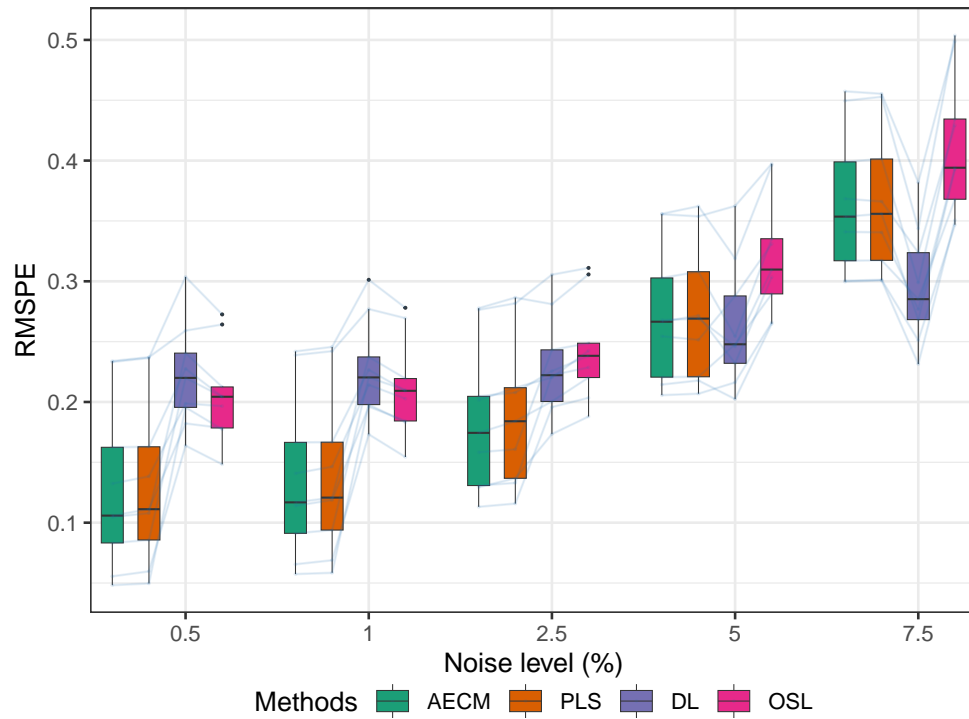


Fig. S3. RMSPE values for different noise of brainweb simulated pictures for different methods for “severe” MS dataset.

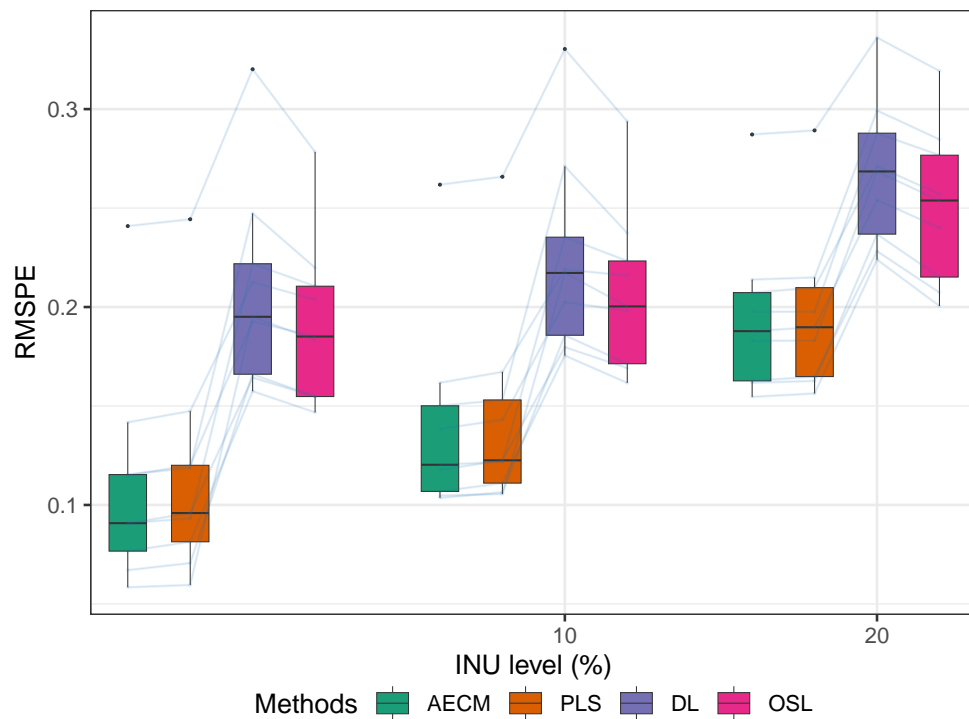


Fig. S4. RMSPE values for different noise of brainweb simulated pictures with respect to different INU levels.